Weierstraß-Institut
für Angewandte Analysis und Stochastik
Leibniz-Institut im Forschungsverbund Berlin e. V.

Preprint ISSN 0946 – 8633

Broadening of mode-locking pulses in quantum-dot semiconductor lasers: simulation, analysis and experiments

Mindaugas Radziunas[1], Andrei G. Vladimirov[1], Evgeny A. Viktorov[2],

Gerrit Fiol[3], Holger Schmeckebier[3], Dieter Bimberg[3]

submitted: December 22, 2010

[1] Weierstrass Institute
Mohrenstr. 39
10117 Berlin, Germany
E-Mail: Mindaugas.Radziunas@wias-berlin.de
Andrei.Vladimirov@wias-berlin.de

[2] Optique Nonlinéaire Théorique
Université Libre de Bruxelles
Campus Plaine CP 231
B-1050 Bruxelles, Belgium
E-Mail: evviktor@ulb.ac.be

[3] Institut für Festkörperphysik
Technische Universität Berlin
Hardenbergstr. 36
10623 Berlin, Germany
E-Mail: gerrit.fiol@physik.tu-berlin.de
schmeckebier@sol.physik.tu-berlin.de
bimberg@physik.tu-berlin.de

No. 1584

Berlin 2010

2010 *Mathematics Subject Classification.* 78A60, 35Q60, 35B30.

2008 *Physics and Astronomy Classification Scheme.* 42.55.Px, 42.60.Fc, 73.63.Kv, 85.30.De, 85.35.Be.

Key words and phrases. mode-locking, semiconductor laser, quantum dots, saturable absorber, pulse broadening, trailing edge .

The work of M. Radziunas was supported by DFG Research Center MATHEON “Mathematics for key technologies: Modelling, simulation and optimization of the real world processes”.

Edited by
Weierstraß-Institut für Angewandte Analysis und Stochastik (WIAS)
Leibniz-Institut im Forschungsverbund Berlin e. V.
Mohrenstraße 39
10117 Berlin
Germany

Fax: +49 30 2044975
E-Mail: preprint@wias-berlin.de
World Wide Web: http://www.wias-berlin.de/

Abstract

We consider a mode-locked quantum-dot edge-emitting semiconductor laser consisting of a reverse biased saturable absorber and a forward biased amplifying section. To describe the dynamics of this laser we use the traveling wave model taking into account carrier exchange processes between a reservoir and the quantum dots. A comprehensive parameter study is presented and an analysis of mode-locking pulse broadening with an increase of injection current is performed. The results of our theoretical analysis are supported by experimental data demonstrating a strong pulse asymmetry in a monolithic two section quantum dot mode-locked laser.

1 Introduction

Semiconductor lasers based on self-assembled quantum dots (QD) [1, 2] attract significant attention due to their improved modulation bandwidth as well as reduced threshold current [3, 4], pulse intensity noise, chirp [5], temperature [6], and feedback sensitivity [7, 8] at telecom wavelengths. The advantages of a QD material can be exploited in multi-section mode-locked (ML) lasers which generate stable high intensity picosecond and even sub-picosecond pulses at high repetition rates [9, 10, 11].

A realistic modeling of QD lasers should take into account carrier exchange processes between a carrier reservoir (CR) and discrete levels in quantum dots. Recently proposed models based on rate equations for QD lasers operating in a continuous wave (CW) regime [12, 13] and delay differential equations (DDE) [14, 15] for QD ML lasers [16] demonstrate a qualitative agreement with some experimental observations. However, these models either neglect spatial distributions of carriers and electric field amplitudes (rate equations), or assume unidirectional lasing in a ring cavity (DDE models). In order to overcome these limitations, we incorporate the carrier exchange rate equations for a QD material (see, e.g., Refs. [17, 18]) into the traveling wave (TW) laser model [19] that takes into account such important features of a ML laser as spatial non-uniformity of laser parameters and spatio-temporal dynamics of carrier densities as well as counter-propagating complex optical fields.

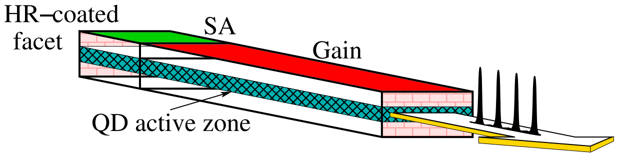

Figure 1: Sketch of a quantum-dot mode-locked laser consisting of a saturable absorber (SA) section and an amplifying (gain) section.

In this paper we consider a model of a two-section QD ML laser consisting of a reverse biased saturable absorber (SA) and a forward biased amplifying (gain) section, see Fig. 1. We perform a comprehensive numerical study of the operation regimes in this laser, identify the type of dynamical states, and estimate different characteristics of ML pulses, such as repetition rate, pulse width (PW) and shape, etc. Special attention is payed to the ML regime with asymmetric pulses [20, 21], and pulses having a broad trailing edge plateau (TEP) [22]. We show that standard approaches for the estimation of the PW of such kind of strongly asymmetric pulses can either lead to controversial results or fail at all.

According to the results of our simulations, the pulses with a broad TEP can appear in different models of QD ML lasers, but they are not typical for related models of quantum-well ML lasers [23]. Our theoretical analysis shows that the TEP in QD ML lasers arises mainly due to non-instant carrier transitions between the CR, excited state (ES), and ground state (GS) of the QD. These multiple finite-time transitions slow-down the carrier exchange between the electrically pumped CR and the photon generating GS of QD, act as a filter, and lead to a homogenization of the carrier and photon distributions along the gain section.

Finally, we support our theoretical findings on the strongly asymmetric pulses having a broad TEP with experimental results performed using the QD ML lasers described in Refs. [24, 21]. We demonstrate that broadening of a pulse with growing injection current results mainly from the growth of its trailing edge. We confirm experimentally that very broad ML pulses whose width at their base exceeds one half of the laser cavity round trip time can appear.

2 Mathematical model

In this section we introduce a 1+1 dimensional TW model governing spatio-temporal evolution of the two counter-propagating optical fields $E^+(z,t)$, $E^-(z,t)$, material polarization functions $p^+(z,t)$, $p^-(z,t)$, normalized carrier density $n_{cr}(z,t)$ within the CR, and occupation probabilities $n_{gs}(z,t) \in [0,1]$ and $n_{es}(z,t) \in [0,1]$ of the GS and ES of quantum dots, respectively.

2.1 Field equations

After fixing a reference wavelength λ_0, the electric field in the laser cavity can be represented as a superposition of two slowly varying complex amplitudes, $E^+(z,t)$ and $E^-(z,t)$, of forward and backward propagating waves. Here, t denotes time and $z \in [0,L]$ is the coordinate along the cavity axis.

The amplitudes $E^\pm(z,t)$ of the two waves counter-propagating in the cavity satisfy the TW equations

$$\frac{\partial}{\partial t}E^\pm = \frac{c_0}{n_{gr}}\left(\mp\frac{\partial}{\partial z} - i\beta - \frac{\mathcal{D}}{2}\right)E^\pm + F^\pm_{sp}, \tag{1}$$

with the reflection boundary conditions at the two laser facets located at $z=0$ and $z=L$

$$E^+(0,t) = r_0 E^-(0,t), \;\; E^-(L,t) = r_L E^+(L,t). \tag{2}$$

Here, c_0 is the speed of light in vacuum, n_{gr} is the group refractive index, $r_{0,L}$ are complex factors describing reflectivity of the laser facets, and $F^\pm_{sp}$ stands for the spontaneous emission noise [25].

The material gain dispersion operator $\mathcal{D}$ describes the frequency dependence of gain profile. Following Ref. [19] we assume that this operator is linear and corresponds to a Lorentzian gain spectrum profile. Furthermore, the inhomogeneous spectral broadening effect due to quantum dot non-uniformity is also neglected in our model. This leads to the following equations for the gain dispersion and material polarization functions $p^+(z,t)$ and $p^-(z,t)$:

$$\mathcal{D}E^{\pm} = \bar{g}\left(E^{\pm} - p^{\pm}\right), \quad \frac{\partial}{\partial t}p^{\pm} = \bar{\gamma}\left(E^{\pm} - p^{\pm}\right) + i\bar{\omega}p^{\pm}, \tag{3}$$

where the parameters $\bar{g}$, $\bar{\omega}$, and $2\bar{\gamma}$ define the height of Lorentzian, its central frequency (relative to $\omega_0 = \frac{2\pi c_0}{\lambda_0}$), and full width at half maximum, respectively.

We will assume that the laser operates at the GS transition only. In this case the propagation factor $\beta(n,z)$ entering Eqs. (1) depends on the ground state occupation probability n_{gs} only:

$$\beta = \beta\left(n_{gs}(z,t), z\right) = \delta - i\frac{\alpha}{2} + \frac{(i - \alpha_H)}{2}g'(2n_{gs} - 1). \tag{4}$$

Here, δ, α, α_H, and g' are the static detuning from the reference wavelength, the internal absorption, the linewidth enhancement factor, and the effective differential gain (including the transverse confinement factor Γ [13]), respectively.

2.2 Material equations

To describe carrier exchange between the CR, GS, and ES of the quantum dots in the gain section (see Fig. 2a) we use the following set of rate equations [17]:

$$\begin{aligned}
\tfrac{d}{dt}n_{gs}(z,t) &= -\tfrac{n_{gs}}{\tau_{gs}} + 2R_{es,gs} - R_{st}(n_{gs}, E), \\
\tfrac{d}{dt}n_{es}(z,t) &= -\tfrac{n_{es}}{\tau_{es}} - R_{es,gs} + R_{cr,es}, \\
\tfrac{d}{dt}n_{cr}(z,t) &= \tfrac{I(z)}{e\theta_I} - \tfrac{n_{cr}}{\tau_{cr}} - 4R_{cr,es}.
\end{aligned} \tag{5}$$

Here, R_{st} is a stimulated recombination term defined by

$$R_{st}(n_{gs}, E) = \tfrac{1}{\theta_E}\Re e\sum_{\nu=\pm}E^{\nu *}(g'(2n_{gs}-1)-\mathcal{D})E^{\nu}, \tag{6}$$

$R_{es,gs}$ and $R_{cr,es}$ are the carrier recombination terms

$$\begin{aligned}
R_{es,gs}(n_{es}, n_{gs}) &= \tfrac{n_{es}(1-n_{gs})}{\tau_{es\to gs}} - \tfrac{n_{gs}(1-n_{es})}{2\tau_{gs\to es}}, \\
R_{cr,es}(n_{cr}, n_{es}) &= \tfrac{n_{cr}(1-n_{es})}{4\tau_{cr\to es}} - \tfrac{n_{es}}{\tau_{es\to cr}},
\end{aligned} \tag{7}$$

while τ_a^{-1} and $\tau_{a\to b}^{-1}$, $a,b \in \{gs, es, cr\}$, denote spontaneous relaxation and transition rates between GS, ES, and CR, respectively. Factors $(1-n_{gs})$ and $(1-n_{es})$ in Eq. (7) represent the Pauli blocking, while factors 2 and 4 in Eqs. (5) and (7) account for the spin degeneracy in the QD energy levels; e is the electron charge and $I(z)$ is the injection current. $I_G = I(z)|_{z\in[l_{SA},L]}$ and $I_{SA} = I(z)|_{z\in[0,l_{SA}]} = 0$ denote injections into the gain and the SA sections, respectively. θ_I and $\theta_E = \frac{2\Gamma c_0 h}{(L-l_{SA})\lambda_0}\theta_I$ (h is the Planck constant) are scaling factors relating the gain section injection current I_G and the field intensity $|E|^2$ with the scaling of n_{cr}, quantum dot density, and the cross-section area of the active zone.

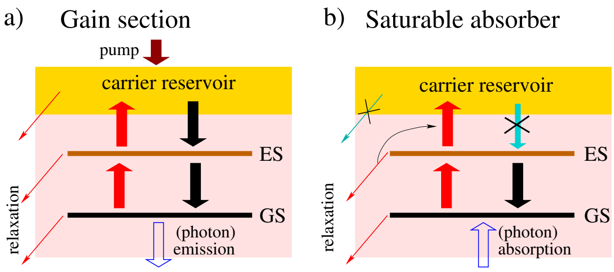

Figure 2: Schematic representation of carrier transitions in the gain section (a) and in the saturable absorber section (b). Crossed arrows in panel (b) indicate the transitions which are neglected in the model equations.

Following [18] we use a simplified carrier rate equation model in the SA section:

$$\begin{aligned} \tfrac{d}{dt} n_{gs}(z,t) &= -\tfrac{n_{gs}}{\tau_{gs}} + 2R_{es,gs} - R_{st}(n_{gs}, E), \\ \tfrac{d}{dt} n_{es}(z,t) &= -\tfrac{n_{es}}{\tau_{es\to cr}} - R_{es,gs}, \quad z \in [0, l_{SA}]. \end{aligned} \tag{8}$$

Here it is assumed that under the reverse bias condition ($z \in [0, l_{SA}]$) the carrier transitions from the CR to the QD ES are neglected in the SA section ($\tau^{-1}_{cr\to es} = 0$, see Fig. 2b). Since in this case the recombination term $R_{cr,es} = -\frac{n_{es}}{\tau_{es\to cr}}$ is independent of n_{cr} and the first two equations in (5) decouple from the third one, this third equation can be ignored. By combining a significantly smaller spontaneous relaxation rate term $n_{es}\tau^{-1}_{es}$ with the term $n_{es}\tau^{-1}_{es\to cr}$, the first two equations in (5) become formally equivalent to Eq. (8).

In our previous theoretical work [22] we have also used a simplified two carrier rate equations model for gain section. In the present paper we will demonstrate how an inclusion of the carrier rate equation for the ES occupation probability n_{es} in the gain section allows to obtain theoretical results on the pulse broadening in ML QD lasers, which are in better agreement with the experimental data.

3 Mode-locking pulsations

We have performed a set of simulations of two-section ML laser schematically represented in Fig. 1 using the TW model (1)-(7) and parameters given in Table 1. The values and more detailed explanation of most of these parameters can be found in Refs. [13, 18, 11] and references therein.

One of the most important parameters of passively ML semiconductor lasers, which can be easily tuned in experiments, is the negative voltage U applied to the SA section. Since, in principle, all the carrier transition rates in Eq. (5) can depend on this parameter, up to now we did not include it into the model equations (1)-(7) explicitly. Below, following Ref. [18], we will assume that all the transition rates but $\tau_{es\to cr}$ are independent of U, while $\tau_{es\to cr}$ shows an exponential dependence on U as given in Table 1.

3.1 Estimation of the pulse width

There is a number of methods to estimate a single pulse width or a mean width of pulses in a train. Below we will compare three different methods to obtain the mean PW.

Table 1:

central wavelength	λ_0	1.3	μm
group refractive index	n_{gr}	3.75	
total length	L	1	mm
SA length	l_{SA}	100	μm
static detuning	δ	0	cm^{-1}
internal absorption	α	5	cm^{-1}
Henry factor	α_H	2	
transversal confinement factor	Γ	0.075	
effective differential gain/absorption	g'	200 / 40	cm^{-1}
Lorentzian height	$\bar{g}$	20	cm^{-1}
Lorentzian peak frequency	$\bar{\omega}$	0	ps^{-1}
Lorentzian width	$2\bar{\gamma}$	1.8	ps^{-1}
CR, ES & GS relaxation rates	$\tau_{cr,es,gs}^{-1}$	0.001	ps^{-1}
ES to GS transition time	$\tau_{es\to gs}$	2	ps
GS to ES transition time	$\tau_{gs\to es}$	5	ps
CR to ES transition rate (SA)	$\tau_{cr\to es}^{-1}$	0	ps^{-1}
CR to ES transition rate (G)	$\tau_{cr\to es}^{-1}$	0.2	ps^{-1}
ES to CR transition time (SA)	$\tau_{es\to cr}$	18 $e^{U/(2V)}$	ps
ES to CR transition time (G)	$\tau_{es\to cr}$	80	ps
injection scaling factor	θ_I	$9.36 \cdot 10^6$	
left facet reflectivity	r_0	$-\sqrt{0.95}$	
right facet reflectivity	r_L	$\sqrt{0.3}$	

First, we estimate the PW as the full-width of the pulse at its half-maximum (FWHM). For almost-periodic pulse train obtained numerically, we sample the pulses with the mean period T_{mean} of this train (see Fig. 3a) and calculate the mean width of these pulses [25, 23]. The main disadvantage of this approach is that it ignores the presence of long non-vanishing pulse tails and satellite pulses with peak powers less then one half of the main pulse peak power.

The *effective* PW (see Fig. 3b) is defined as the width of a rectangular pulse having the same peak power P_{max} and the same energy as the original pulse:

$$PW_{eff} = \frac{T_{mean} P_{mean}}{P_{max}}, \tag{9}$$

where P_{mean} is the mean power of the emitted field. This definition is easy to understand at an intuitive level and it accounts for the wings of the pulse. However, the PW estimations performed using this method become inadequate when the decay rate of the wings is too small, and especially when the field power between two subsequent pulses in the train does not drop to zero.

A common approach to estimate the PW is based on the evaluation of the FWHM of the auto-correlation (AC) function

$$AC(\tau) = \int P(t)P(t-\tau)dt \ \Big/ \int P^2(t)dt$$

of the emitted field intensity $P(t)$ (see Fig. 3c). Usually the width of the AC function is broader then the width of the original pulse by the so-called deconvolution factor. It is equal to $\sqrt{2}$ for a Gaussian pulse profile, and ≈ 1.54 for a hyperbolic secant squared ($sech^2$) pulse. In addition, unlike the original pulse profile the AC function is always symmetric, see panels (a) and (c) of Fig. 3.

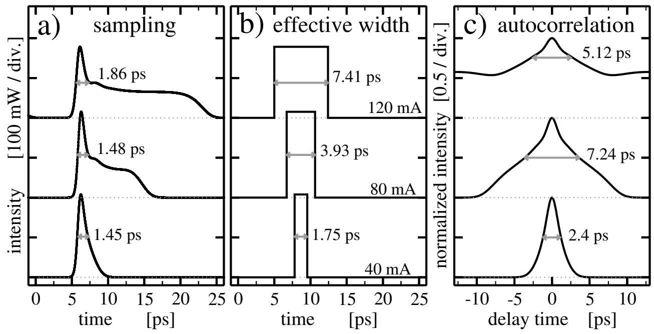

Figure 3: Sampling diagrams (a), rectangular pulse reconstructions (b), and autocorrelation functions (c) of the ML pulsations. Parameters $U = -3$V, $I_G = 40$mA (below), $I_G = 80$mA (middle), and $I_G = 120$mA (above).

It follows from Fig. 3 that the result of the PW estimation depends strongly on the pulse shape and the method used. While for weakly asymmetric pulses such as, for example, discussed in [20] all the three approaches mentioned above give more or less similar results (see lower curves of Fig. 3), for the ML pulses with a large TEP (two upper curves in Fig. 3a) the PW calculated by different methods differ significantly. In general case, none of these three methods alone is able to provide a satisfactory information about the width of strongly asymmetric ML pulses.

4 One- and two- parameter study

To get a more systematic insight into the dynamics of the ML laser equations introduced in Sec. 2 we have performed one- (injection current) and two- (voltage/current) parameter study of these equations. For identification and characterization of different ML regimes and other dynamical states automatic routines, based on estimation of the radio-frequency spectra, sampling diagrams, and AC functions of the emitted optical field [25, 23, 22], have been used. We note, however, that these routines work well only for regular fundamental ML regime, but they can provide less reliable or even wrong results in the case of Q-switched ML or irregular quasi- or non-periodic pulse train.

Fig. 4 shows numerically calculated diagrams illustrating a typical sequence of operation states which appear with the increase of the injection current I_G. Below the lasing threshold ($I_G \leq I_{thr} \approx 9$mA) the laser is off, as it is indicated by zero field intensity in panel (a) of this figure. Above the lasing threshold for $I_{thr} < I_G < 35$mA the laser operates in a Q-switched ML regime [23] characterized by the pulse bunches emitted periodically with the Q-switching frequency ($1 \div 4$ GHz). We note, that for different values of model parameters (e.g., ratio of differential gain factors g' in the gain and SA sections) a bistability between the fundamental ML regime and non-lasing state [27] can be observed above the lasing threshold. At higher injection currents the fundamental ML regime appears: see the lower curve in Fig. 3a. Within

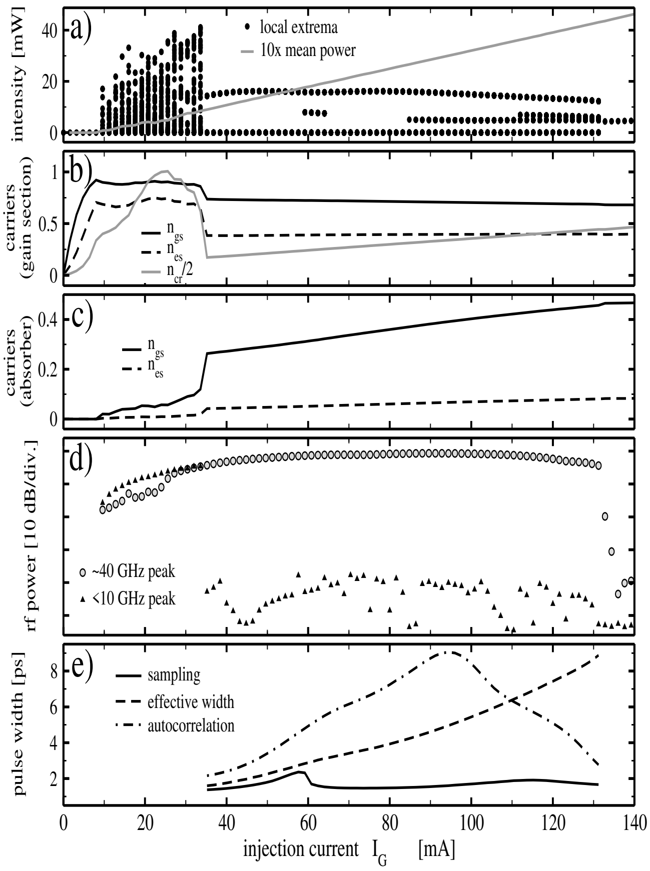

Figure 4: Calculated one-parameter diagrams illustrating the dependence of different characteristics of ML regime on the injection current I_G. Absorber voltage is fixed, $U = -3$V. (a): Local minima and maxima (bullets) and time-averaged value (solid gray line) of electric field intensity $|E^+(L,t)|^2$. (b): Time and space-averaged occupation probabilities n_{gs}, n_{es}, and carrier density n_{cr} in the amplifier section. (c): Time and space-averaged occupation probabilities n_{gs} and n_{es} in the SA section. (d): Peak intensity of fundamental ML (bullets) and low-frequency oscillations (triangles) in the radio-frequency spectra. (e): Width of ML pulses according to FWHM of the sampling diagrams (solid), autocorrelation functions (dash-dotted) and rectangular pulse reconstructions (dashed).

the injection range where the fundamental ML regime is stable, the peak power of the emitted pulses remains nearly independent of I_G, see upper dots in Fig. 4a. The linearly increasing averaged field intensity represented by a grey line in the same panel corresponds to a formation of the TEP (the middle curve in Fig. 3a), and its broadening with a consequent creation of a few weakly pronounced additional local extrema (see upper curve in Fig. 3a and the middle-intensity bullets in Fig. 4a). According to our recent study of the TEP formation [22, 26], these additional extrema indicate an interference of two groups of the locked modes. Finally, for $I_G > 132$mA the ML is lost and a transition to continuous wave regime occurs.

It is seen from Fig. 4b, that within the stability range of the fundamental ML regime the mean carrier density n_{cr} in the CR of the gain section increases almost linearly with the injection current. The mean occupation probability of the ground state n_{gs} in the SA section (Fig. 4c) shows a similar linear increase due to the growing mean power of ML pulses. At the same time, the population of the exited state n_{es} in the SA section increases with I_G only slightly (panel c), while n_{gs}, n_{es} in the gain section remain almost independent of the injection current (panel b).

Panel (d) of Fig. 4 shows several characteristics of ML regime which have been extracted from the radio-frequency spectra. Triangles and bullets in Fig. 4d indicate the intensities of the biggest spectral peak within small $[0, 10]$ GHz frequency range and the intensities of the peak corresponding to the fundamental ML frequency ~ 40GHz, respectively. The ML frequency peak is clearly visible even at small injection currents, just after switching the laser on. It degrades significantly only at sufficiently high injections corresponding to the continuous wave operation of the laser. The low-frequency peak, which dominates in the Q-switched ML regime, becomes strongly suppressed with the increase of the injection current when a transition to a stable fundamental ML regime takes place.

Fig. 4e represents different estimates of the pulse width. The PW estimated from the sampling diagrams (solid curve) represents a nearly constant 1.6 ± 0.2ps width of the sharp peak of the pulse, see also Fig. 3a. For the injection currents around $I_G \approx 58$mA and $I_G \approx 115$mA the front part of the TEP exceeds the half-height level of the main pulse. This leads to a slight increase of the PW, see upper curve in Fig. 3a. The dash-dotted curve in Fig. 4e represents the PW estimation from the FWHM of the AC function. It grows monotonously with the injection current, achieves its maximum at $I_G \approx 95$ mA, and then starts to decrease. At such high injection currents the TEP width exceeds the half of the pulse repetition period T_{mean}, and, as a result of this, the wings of the corresponding AC function do not decay to zero any more, see, e.g., upper curve in Fig. 3c. It reduces the effective height of the AC function, and leads to the decay of the AC width which is measured at its half height.

Finally, the effective PW measured according to the formula (9) increases monotonously with the injection current, see dashed line in Fig. 4e. This can be explained by the linear increase of the mean power P_{mean} (grey curve in Fig. 4a).

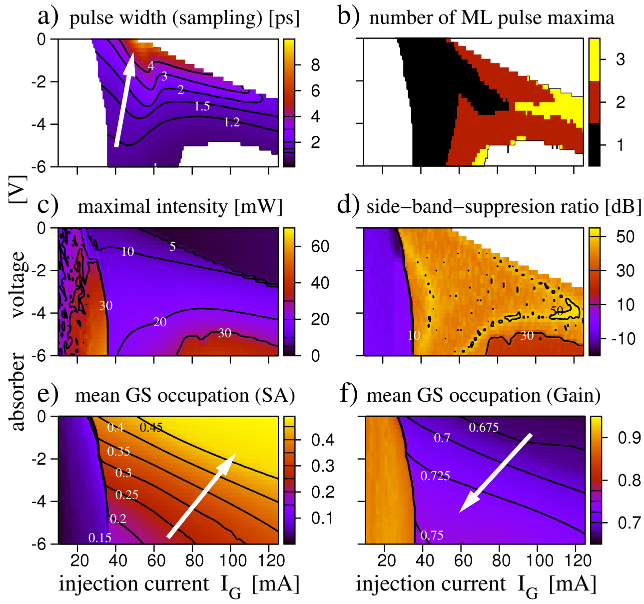

Figure 5: Two-parameter analysis of the ML laser model. Pulse width (a) and number of local maxima (b) within ML pulse are shown for regular periodic ML regimes. A low frequency spectral peak suppression with respect to the peak of the fundamental ML (side-band-suppresion ratio, panel d) is presented only for non-stationary solutions. Black curves in all diagrams are the isolines showing fixed values of a corresponding function.

Some results of two-parameter simulations are summarized in Fig. 5, which illustrates the dependence of different characteristics of ML regime on the injection current I_G and the absorber voltage U. The first two panels (a) and (b) of this figure represent characteristics of the regular periodic ML regime. They have been obtained by analyzing sampling diagrams (see Fig. 3a and Refs. [25, 23]). The parameter regions corresponding to the white areas in these panels correspond to non-ML regimes of operation. To the left from the ML region we have the laser off state and a regime with irregular pulse train of the Q-switching type. At the upper right corner the laser operates in a continuous wave regime, while the lower right corner corresponds to an irregular ML pulse train with strongly varying peak amplitude and pulse shape.

A significant increase of the PW with the injection at small and moderate negative voltages in panel (a) is due to the broadening of the TEP whose peak power exceeds one half of the main pulse peak power. It is also seen from this panel that the PW decreases with the increase of the absolute value of negative voltage applied to the SA section. Panel (b) represents the number of the distinguishable local maxima within a single pulse. According to this diagram, an increase of the injection current leads to the formation of additional maxima at the top of the TEP [22, 26]. The maximal intensity diagram in panel (c) shows some growth (from ~ 6mW to ~ 24mW) of P_{max} with the increase of the voltage $|U|$. According to this panel the main pulse peak power is only weakly dependent on the injection current within the parameter domain of regular ML regime.

Panel (d) represents a side-band-suppression ratio of non-stationary lasing regimes. We define this ratio as the difference between the fundamental ML peak amplitude and the maximal low frequency peak amplitude in the power spectrum (see also separation between bullets and triangles in Fig. 4d). While the signal to noise ratio is $\sim 35 \div 55$ dB for regular ML pulsations, it changes to ~ 20 dB for irregular and modulated ML pulsations (lower right corner) and becomes negative for Q-switching type pulsations.

Panels (e) and (f) of Fig. 5 show the time-averaged GS occupation probability n_{gs} in the SA section and the gain section, respectively. It is seen from the panel (e) that within the Q-switching domain corresponding to small injection currents the averaged occupation probability n_{gs} of the GS in the absorber section is rather small, and, therefore, the absorber is weakly saturated. Low saturation requires a relatively high amplification in the gain section. Therefore, the values of the averaged GS occupation probability n_{gs} in this section are relatively high, see panel (f). Transition to a regular ML regime leads to an increase of the absorption saturation in the SA section and, hence, to an increase of the averaged value of n_{gs} in this section, see panel (e) of Fig. 5. Within the ML domain the averaged absorber GS occupation probability n_{gs} increases with the decrease of the voltage $|U|$ (i.e. with the increase of the carrier escape time $\tau_{es\to cr}$) and with the increase of the injection current. This leads to a growth of ML pulse energy. A corresponding small decrease of the averaged occupation probability of the ground state in the gain section is visible in panel (f).

At the upper right border of the ML region the existence of a broad TEP behind the main pulse keeps the absorption strongly saturated during almost the whole pulse round-trip time. After crossing this border the ML is lost and a transition to a continuous wave state with only slightly higher absorption saturation occurs.

5 Impact of intra-dot relaxation dynamics

The fundamental ML regime is usually characterized by a single short pulse circulating within the laser cavity. An increase of the injection current leads to a growth of the photon number. Depending on laser parameters, the optical field power either remains concentrated within one or several short pulses, or spreads over a significant part of the cavity axis. The first situation is rather typical for ML lasers; it was discussed, e.g., in [14, 15, 23, 28, 22]. In this case, the peak power of the emitted fundamental ML pulse grows with the injection current and above a certain threshold can split into two or more short pulses with smaller peak power. Harmonic mode-locking [14, 15, 23] with two or more identical and equidistant pulses circulating in the cavity is a particular case of such field intensity localization in the longitudinal direction.

Operation regimes with less localized or even homogeneous distribution of the electric field intensity in the cavity are also common in the considered lasers. For example, a continuous wave lasing is usually observed at sufficiently large current injections. A less typical example is a ML regime with a large TEP (see upper curves in Fig. 3a) first reported in Ref. [22], where a simplified carrier exchange model with only a single discrete level of QDs in the gain section was used. It is noteworthy, that while a fundamental ML pulse peak intensity growth and a transition to two-pulse states were still observable in the model equations studied in [22], such states have not been found in the present study. For the model equations described in Section 2 an increase of the pumping level leads to a smooth transformation of a regular fundamental ML regime into a ML regime with a large TEP, see Fig. 4a.

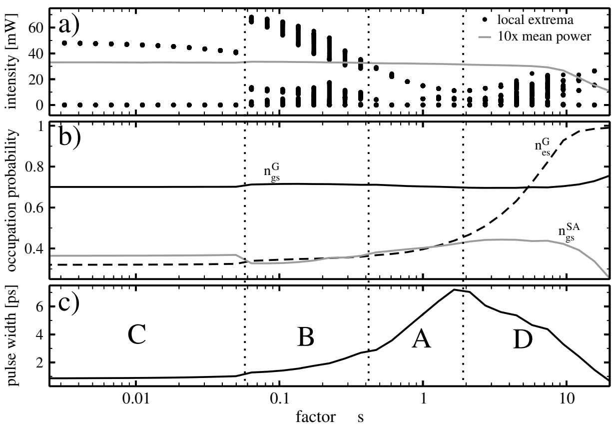

Figure 6: Evolution of ML regimes with the parameter s defined by Eq. (10). $U = -3$V and $I_G = 100$mA. (a): Local minima and maxima (bullets) and time-averaged value (curve) of the output field intensity. (b): Time and space-averaged occupation probabilities n_{gs}, n_{es} in the gain section (black solid and dashed) and n_{gs} in the SA section (grey). (c): Effective width of ML pulses defined by Eq. (9). A to D: different operating regimes of the laser.

The formation of a long TEP instead of a small secondary pulse or harmonic ML pulses traveling in the laser cavity can be understood by noticing the fact that the multiple carrier rate equations (5) impose some filtering effect, which leads to a homogenization of the carrier and photon distributions along the gain section. To illustrate this effect related to the rate equation for the occupation probability of the ES we have performed a set of simulations with the carrier transition times between the GS and ES in the gain section varied according to the relations

$$\tau_{es\to gs} = s\tau^0_{es\to gs}, \quad \tau_{gs\to es} = s\tau^0_{gs\to es}, \tag{10}$$

where $\tau^0_{es\to gs}$ and $\tau^0_{gs\to es}$ are the transition times given in Table 1, and s is a tuning parameter.

The results of these simulations are summarized in Fig. 6, where the extrema and the averaged power of the emitted field (a), the averaged values of several carrier functions (b), and the effective PW (c) are presented for different values of the parameter s. The PW estimation have been performed using the procedure based on Eq. (9).

Four different operating regimes can be distinguished in Fig. 6. In the region A we have a ML regime with a TEP. An increase (decrease) of the factor s from its original value $s = 1$ results in growing (shrinking) of the TEP width, see PW represented in panel (c). Region B corresponds to a ML regime with a modulated peak power of both the main pulse and the TEP. At the left boundary of this region the TEP separates from the main peak forming a small secondary pulse. The existence of such double-pulse ML state in a two times longer QD ML laser was demonstrated experimentally in [28]. In the region C we have a harmonic ML regime with two identical pulses circulating in the cavity. This regime corresponding to the pulse repetition frequency close to 80 GHz was a typical feature of the laser equations with the simplified gain section model studied in Ref. [22]. When the parameter s decreases, the transitions between the ES and GS become faster, the filtering effect becomes weaker, and, therefore, localization of the carrier and photon distributions becomes stronger. In Fig. 6 this is illustrated by growth of ML peak amplitude within the region B and decay of the pulse width within the regions A, B and C.

The region D corresponds to $s > 1$ and, hence, the transitions between the GS and ES are slowed down in this region. Formally, this means that the filtering leading to TEP broadening becomes stronger. On the other hand, the terms $R_{es,gs} > 0$ in Eqs. (5) serve as a source of positive (negative) pumping for the GS (ES). With the decrease of this term, the averaged ES occupation probability n_{es} in the gain section grows (see dashed curve in panel b). Since the GS occupation probability n_{gs} in the gain section remains nearly constant (see solid black curve in panel b), the decay of the GS pumping term $R_{es,gs}$ implies a decrease of the time-averaged output field intensity (see grey curve in panel a). This, in turn, leads to a weaker SA section saturation, i.e. to a decrease of the GS occupation probability (see gray curve in panel b), and, finally, to a slight rise of n_{gs} (or threshold gain) in the gain section (see the right side of the black curve in panel b). When the GS pump term $R_{es,gs}$ becomes too small, the laser switches off.

6 Experiments

The above discussed pulse broadening has been also observed experimentally. Experimental studies have been performed with a ridge waveguide (4μm ridge width) monolithic two section QD ML laser. The material incorporated is InGaAs forming 15 stacked layers of QDs.

The device was integrated in a module comprising a fiber pigtail, a microwave port, dc contacts, and a thermoelectric cooler. Basic properties like PIV-curves, repetition frequency, pulse width/pulse shape dependencies on operating parameters, temperature dependencies as well as the characteristics of hybrid ML are already published in [24, 21, 27, 30].

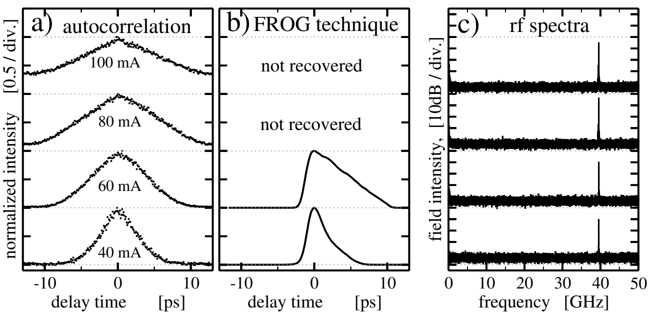

Figure 7: Experimental representation of ML pulsations for fixed voltage $U = -3.5V$ and several injection currents I_G. (a): Autocorrelation functions. (b): Pulse reconstructions using FROG technique. (c): Radio-frequency spectra.

The results of the experiments are presented in Fig. 7 for several values of injection currents I_G. The autocorrelations (panel a) have been measured using a second-harmonic generation setup [31] incorporating a $LiNbO_3$ crystal. Normalization of the autocorrelation functions was performed after removal of a measurement equipment induced background noise. Actually, similar corrections were used when performing FROG measurements (panel b) as well as when representing the radio-frequency spectra (panel c). Note that ~ 25 ps time intervals used for representation of the AC and FROG measurements in panels (a) and (b) correspond to the pulse round trip time in the cavity.

The AC functions of the ML pulses (panel a) clearly show a typical increase of the PW with increasing injection currents. Note that for $I_G \geq 80$mA the AC function has non-vanishing wings, what is typical for pulses remaining distinguishable from zero for more then the half period of the pulsations (compare with the upper curve in Fig. 3c). For the CW state the AC function would be almost flat.

Fig. 7b shows the corresponding pulses reconstructed by means of the FROG technique [21, 29]. Similarly to our theoretical Fig. 3a, the front edge of the pulse remains nearly independent on I_G, while its broadening is due to the growing trailing edge of the pulse. Looking at the results for 40 and 60 mA one can recognize the formation of the TEP. For even higher injection, however, the pulse reconstructions have failed, since the FROG algorithm requires zero intensities at the edges of the corresponding AC functions.

Fig. 7c shows the radio-frequency (rf) spectra corresponding to the states discussed in panels (a) and (b). We note, that all rf spectra are, in general, the same: they posses a large peak at the fundamental ML frequency and have suppressed low frequency peaks.

The similarity of the rf spectra and the absence of any visible bifurcations while increasing I_G lead to the conclusion that even for high $I_G = 100mA$ the laser operates at a ML pulsating state. A drastic broadening of the pulse (its TEP) does not allow here to recover a pulse shape by means of the AC or the FROG technique.

7 Conclusions

We have performed a numerical study using a TW model of a ML QD laser consisting of a reversely biased saturable absorber and a forward biased gain section. This model is based on equations governing the spatio-temporal evolution of the amplitudes of two counter-propagating waves in the cavity coupled to the rate equations describing carrier exchange processes between a carrier reservoir and discrete levels in quantum-dots. Different dynamical regimes of laser operation are analyzed. We have demonstrated theoretically that an increase of the injection current can lead to formation of ML pulses possessing a large TEP. We explain the formation and broadening of the TEP by the filtering effect associated with non-instant carrier transitions between the CR, ES and GS of the QDs. Furthermore, we demonstrate how a drastic broadening of the TEP can lead to the failure of the standard techniques used for estimation of the pulse width. Finally, we have provided experimental evidence of the existence of such kind of regimes in QD ML lasers.

Acknowledgments

The work of M. Radziunas was supported by DFG Research Center MATHEON "Mathematics for key technologies: Modelling, simulation, and optimization of real-world processes". E. A. Viktorov acknowledges Science Foundation Ireland for the Walton Fellowship Award 08/W.1/I2589. A. G. Vladimirov and the authors from TU Berlin acknowledge the support from SFB 787 project of the DFG.

References

[1] N.N. Ledentsov, D. Bimberg, and Zh.I. Alferov, "Progress in epitaxial growth and performance of quantum dot and quantum wire lasers," *J. Lightwave Technol.* **26**, pp. 1540–1555, 2008.

[2] N. Kirstaedter, N.N. Ledentsov, M. Grundmann, D. Bimberg, V.M. Ustinov, S.S. Ruvimov, M.V. Maximov, P.S. Kopev, Z.I. Alferov, U. Richter, P. Werner, U. Gosele, J. Heydenreich, "Low-threshold, large T_O injection-laser emission from (InGa)As quantum dots," *Electron. Lett.* **30**(17), pp. 1416–1417, 1994.

[3] G. Park, O.B. Shchekin, D.L. Huffaker, and D.G. Deppe, "Low-threshold oxide-confined 1.3-μm quantum-dot laser," *IEEE Photonic. Tech. L.* **12**, pp. 230–232, 2000.

[4] D. Bimberg, "Quantum dot based nanophotonics and nanoelectronics," *Electron. Lett.* **44**(3), pp. 168–170, 2008.

[5] H. Saito, K. Nishi, A. Kamei, and S. Sugou, "Low chirp observed in directly modulated quantum dot lasers," *IEEE Photonic. Tech. L.* **12**, pp. 1298–1300, 2000.

[6] R. Debusmann, T.W. Schlereth, S. Gerhard, W. Kaiser, S. Höfling, and A. Forchel, "Gain studies on quantum-dot lasers with temperature-stable emission wavelength," *IEEE J. Quantum Elect.* **44**, pp. 175–181, 2008.

[7] D. O'Brien, S.P. Hegarty, G. Huyet, and A.V. Uskov, "Sensitivity of quantum-dot semiconductor lasers to optical feedback," *Opt. Lett.* **29**, pp. 1072–1074, 2004.

[8] G. Huyet, D. O'Brien, S.P. Hegarty, J.G. McInerney, A.V. Uskov, D. Bimberg, C. Ribbat, V.M. Ustinov, A.E. Zhukov, S.S. Mikhrin, A.R. Kovsh, J.K. White, K. Hinzer, A.J. SpringThorpe, "Quantum dot semiconductor lasers with optical feedback," *Phys. Status Solidi A* **201**(2), pp. 345–352, 2004.

[9] E.U. Rafailov, M.A. Cataluna, and W. Sibbett, "Mode locked quantum-dot lasers," *Nat. Photonics* **1**, pp. 395–401, 2007.

[10] M.G. Thompson, A.R. Rae, Mo Xia, R.V. Penty, I.H. White, "InGaAs quantum dot mode-locked laser diodes," *IEEE J. Sel. Top. Quant.* **15**, pp. 661–672, 2009.

[11] M. Kuntz, G. Fiol, M. Laemmlin, C. Meuer, and D. Bimberg "High-speed mode-locked quantum-dot lasers and optical amplifiers," *Proc. IEEE* **95(9)**, pp. 1767–1778, 2007.

[12] A. Markus, J.X. Chen, O. Gauthier-Lafaye, J.-G. Provost, C. Paranthoën, and A. Fiore, "Impact of intraband relaxation on the performance of a quantum-dot laser," *IEEE J. Sel. Top. Quant.* **9**, pp. 1308–1314, 2003.

[13] K. Lüdge and E. Schöll, "Quantum-dot lasers – desynchronized nonlinear dynamics of electrons and holes," *IEEE J. Quantum Elect.* **45**, pp. 1396–1403, 2009.

[14] A.G. Vladimirov, D. Turaev, and G. Kozyreff, "Delay differential equations for mode-locked semiconductor lasers," *Opt. Lett.* **29**, pp. 1221–1223, 2004.

[15] A.G. Vladimirov and D. Turaev, "Model for passive mode-locking in semiconductor lasers," *Phys. Rev. A* **72**, p. 033808, 2005.

[16] E.A. Viktorov, P. Mandel, A.G. Vladimirov, and U. Bandelow, "A model for mode-locking in quantum dot lasers," *Appl. Phys. Lett.* **88**, p. 201102, 2006.

[17] A. Markus, M. Rossetti, V. Calligari, D. Chek-Al-Kar, J.X. Chen, and A. Fiore, "Two-state switching and dynamics in quantum dot two-section lasers," *J. Appl. Phys.* **100**(1), p. 113104, 2006.

[18] E.A. Viktorov, T. Erneux, P. Mandel, T. Piwonski, G. Madden, J. Pulka, G. Huyet, and J. Houlihan, "Recovery time scales in a reversed-biased quantum dot absorber," *Appl. Phys. Lett.* **94**, p. 263502, 2009.

[19] U. Bandelow, M. Radziunas, J. Sieber, and M. Wolfrum, "Impact of gain dispersion on the spatio-temporal dynamics of multisection lasers," *IEEE J. Quantum Elect.* **37**, pp. 183–188, 2001.

[20] N.G. Usechak, Yongchun Xin, Chang-Yi Lin, L.F. Lester, D.J. Kane, and V. Kovanis "Modeling and direct electric-field measurements of passively mode-locked quantum-dot lasers," *IEEE J. Sel. Top. Quant.* **15**, pp. 653–660, 2009.

[21] H. Schmeckebier, G. Fiol, C. Meuer, D. Arsenijevic, and D. Bimberg, "Complete pulse characterization of quantum-dot mode-locked lasers suitable for optical communication up to 160 Gbit/s," *Opt. Express* **18**, pp. 3415–3425, 2010.

[22] M. Radziunas, A.G. Vladimirov, and E.A. Viktorov, "Traveling wave modeling, simulation and analysis of quantum-dot mode-locked semiconductor lasers," *Proc. of SPIE* **7720**, p. 77200X, 2010.

[23] U. Bandelow, M. Radziunas, A. Vladimirov, B. Hüttl, and R. Kaiser, "Harmonic mode-locking in monolithic semiconductor lasers: theory, simulations and experiment," *Opt. Quant. Electron.* **38**, pp. 495–512, 2006.

[24] G. Fiol, C. Meuer, H. Schmeckebier, D. Arsenijevic, S. Liebich, M. Laemmlin, M. Kuntz, and D. Bimberg, "Quantum-dot semiconductor mode-locked lasers and amplifiers at 40 GHz," *IEEE J. Quantum Elect.* **45**, pp. 1429–1435, 2009.

[25] H.-J. Wünsche, M. Radziunas, S. Bauer, O. Brox, and B. Sartorius, “Simulation of phase-controlled mode-beating lasers,” *IEEE J. Sel. Top. Quant.* **9**, pp. 857–864, 2003.

[26] M. Radziunas, A.G. Vladimirov, E. Viktorov, G. Fiol, H. Schmeckebier, and D. Bimberg, “Strong pulse asymmetry in quantum-dot mode-locked semiconductor lasers,” *submitted*.

[27] A.G. Vladimirov, U. Bandelow, G. Fiol, D. Arsenijević, M. Kleinert, D. Bimberg, A. Pimenov, and D. Rachinskii, “Dynamical regimes in a monolithic passively mode-locked quantum dot laser,” *J. Opt. Soc. Am. B* **27**, pp. 2102–2109, 2010.

[28] E.A. Viktorov, P. Mandel, M. Kuntz, G. Fiol, D. Bimberg, A.G. Vladimirov, and M. Wolfrum “Stability of the mode-locked regime in quantum dot lasers,” *Appl. Phys. Lett.*, **91** p. 231116, 2007.

[29] D.J. Kane and R. Trebino “Characterization of arbitrary femtosecond pulses using frequency-resolved optical gating,” *IEEE J. Quantum Elect.* **29**, pp. 571–579, 1993.

[30] G. Fiol, D. Arsenijevic, D. Bimberg, A.G. Vladimirov, M. Wolfrum, E.A. Viktorov and P. Mandel, “Hybrid mode-locking in a 40 GHz monolithic quantum dot laser, ” *Appl. Phys. Lett.* **96**, p. 011104, 2010.

[31] H.P. Weber, “Method for pulsewidth measurement of ultrashort light pulses generated by phase-locked lasers using nonlinear optics,” *J. of Appl. Phys.* **38**, pp. 2231–2234, 1967.